

Pressure-Induced Enhancement of Thermoelectric Figure of Merit and Structural Phase Transition in TiNiSn

Jason L. Baker, Changyong Park, Curtis Kenney-Benson, Vineet Kumar Sharma, V. Kanchana, G. Vaitheeswaran, Chris J. Pickard, Andrew Cornelius, Nenad Velisavljevic, and Ravhi S. Kumar*

Cite This: *J. Phys. Chem. Lett.* 2021, 12, 1046–1051

Read Online

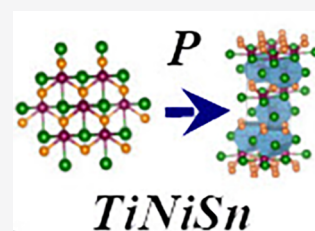
ACCESS |

Metrics & More

Article Recommendations

Supporting Information

ABSTRACT: Half-Heusler thermoelectric materials are potential candidates for high thermoelectric efficiency. We report high-pressure thermoelectric and structural property measurements, density functional theory calculations on the half-Heusler material TiNiSn, and an increase of 15% in the relative dimensionless figure of merit, ZT, around 3 GPa. Thermal and electrical properties were measured utilizing a specialized sample cell assembly designed for the Paris–Edinburgh large-volume press to a maximum pressure of 3.5 GPa. High-pressure structural measurements performed up to 50 GPa in a diamond-anvil cell indicated the emergence of a new high-pressure phase around 20 GPa. A first-principles structure search performed using an ab initio random structure search approach identified the high-pressure phase as an orthorhombic type, in good agreement with the experimental results.



As global energy production continually increases, it becomes of ever-increasing importance to research, identify, synthesize, and characterize materials that can provide a renewable and reliable source of energy and waste heat recovery.¹ One such class of materials are thermoelectric materials, which enable the conversion of heat energy via a thermal gradient into electrical energy without a reliance on moving parts. Thermoelectric materials have long provided industrial energy solutions for specific applications, such as power through radio-isotope thermoelectric generators used by NASA on several space-faring missions.² Although these materials have the potential to provide a reliable method of energy production and reduction of waste heat energy, their practical application is highly dependent on their efficiency. This efficiency is defined through a dimensionless figure of merit (ZT),

$$ZT = \frac{\alpha^2 \sigma}{\kappa} T \quad (1)$$

where α , σ , T , and κ are the Seebeck coefficient, electrical conductivity, absolute temperature, and thermal conductivity, respectively. A larger value for ZT indicates a material with a greater thermoelectric efficiency. As eq 1 implies, a larger efficiency (at a constant temperature) strongly depends on having a large Seebeck coefficient, a high electrical conductivity, and a low thermal conductivity.

Several classes of thermoelectric materials are of high interest, such as half-Heusler compounds,^{3–9} filled skutterdites,^{10,11} nanostructured alloys,^{11,12} binary chalcogenides,^{13,14} and others.^{15–17} Of particular interest among these classes of materials are the half-Heusler compounds due to their typically high Seebeck coefficient and generally good electrical

conductivity.^{3–9} However, these materials tend to have fairly large thermal conductivity, which, according to eq 1, would decrease ZT in these materials. Research has been dedicated to identifying methods to reduce the thermal conductivity of these materials while ideally retaining or increasing the Seebeck coefficient and electrical conductivity. The MNiSn family of half-Heusler alloys has been extensively studied with the goal set to increase their ZT value.^{18–22} These materials exhibit a very high Seebeck coefficient at room temperature conditions, reaching values of over $-200 \mu\text{VK}^{-1}$.^{19–24} Bhattacharya et al. have reported an increase in the power factor ($\sigma\alpha^2$) with a small amount of Sb doping at the Sn site of TiNiSn through a large decrease in the electrical resistivity despite a decrease in the Seebeck coefficient.¹⁹ Other studies have shown a strong effect on the thermoelectric properties during the synthesis process when spark plasma sintering (SPS) was performed at various temperatures.²¹ Kurosaki et al. performed SPS on $(\text{Zr}_{0.6}\text{Hf}_{0.4})_{0.7}\text{Ti}_{0.3}\text{NiSn}$ at 973, 1173, and 1373 K and observed optimal thermoelectric efficiency in the sample prepared at 1173 K.²¹ Even though a decrease in the power factor was reported, a decrease of 70% in the thermal conductivity leads to a ZT value of 0.43 at 760 K.²¹ Similar to other half-Heusler compounds, MNiSn materials exhibit large thermal conductivity, and without proper reduction of these large values, their applicability to devices is limited.

Received: December 7, 2020

Accepted: January 7, 2021

Published: January 20, 2021



To further optimize the thermoelectric efficiency of these materials, continued effort is required to identify and characterize new phases and understand the transport behavior in a variety of conditions (i.e., temperature, pressure). Both pressure and temperature can significantly alter the thermal, electrical, and structural properties of materials and specifically have shown a positive effect on thermoelectric efficiency in several studies.^{25–29} PbTe and other chalcogenides have shown large changes in electrical resistivity and power factor with application of modest pressures.²⁵ Recently, Baker et al. studied the thermoelectric behavior of SnTe at high-pressure conditions and observed a significant increase in Seebeck coefficient over the pressure range studied. Due to the potential access to high-pressure phases and unique behavior of materials under high-pressure conditions, studying the electrical, thermal, and structural properties of TiNiSn as a function of pressure is important.

The high-pressure structural and thermoelectric behavior of TiNiSn has not been investigated experimentally. To determine the importance of pressure as a method for tuning the transport properties of materials and identify new phases of materials with potentially favorable thermoelectric properties, it is imperative to study this material at high P – T conditions. Theoretical studies have been conducted by Wang et al., who predicted values for the bulk modulus of TiNiSn utilizing the Birch–Murnaghan equation of state (BM-EOS) as a model.¹⁸ In a comparison study of the full-Heusler compound TiNi₂Sn and half-Heusler compound TiNiSn, Hermet et al. compared the mechanical and structural properties of these materials based on the Young's and shear moduli and the bulk modulus for these materials.³⁰ To this date, there are no theoretical or experimental studies of the high-pressure thermoelectric and structural behavior of TiNiSn.

In this Letter, we report the synthesis, high-pressure powder X-ray diffraction (HP-XRD), high-pressure electrical and thermal measurements, and density functional theory (DFT) calculations on TiNiSn and the onset of a pressure-induced structural phase transition around 20 GPa to an orthorhombic structure described by space group $Cmcm$ (No. 63). In the high-pressure electrical and thermal experiments, we have measured the electrical resistance, Seebeck coefficient, relative change in the thermal conductivity, and relative changes to the dimensionless figure of merit, ZT , of TiNiSn up to 3.5 GPa. A significant enhancement of the thermoelectric efficiency over this pressure range was observed.

The refined structural unit cell parameters for the cubic phase for TiNiSn are $a = b = c = 5.933(1)$ Å, as determined by a Rietveld refinement performed on ambient-pressure XRD data, Figure S1, which agrees well with the literature values.^{22,31} This is also in good agreement with the Generalized Gradient Approximation (GGA) calculations performed as part of this study. Atomic positions for all atom locations in the unit cell for the ambient cubic crystal structure described by the $F\bar{4}3m$ space group (No. 216) are fixed due to symmetry conditions. Figure 1 depicts the evolution of the XRD patterns with increasing pressure.

The expected shift to higher 2θ angles with increasing pressure is clearly visible over the entire pressure range. Below 20 GPa, the sample remains in the cubic structure and displays no significant changes in the XRD patterns. Around 20 GPa, we observe changes in the diffraction patterns. Low-intensity peaks start to emerge around 2θ angles 5.4° , 6.7° , 8.5° , and 11.1° . The splitting of the diffraction peak around 8.5° is

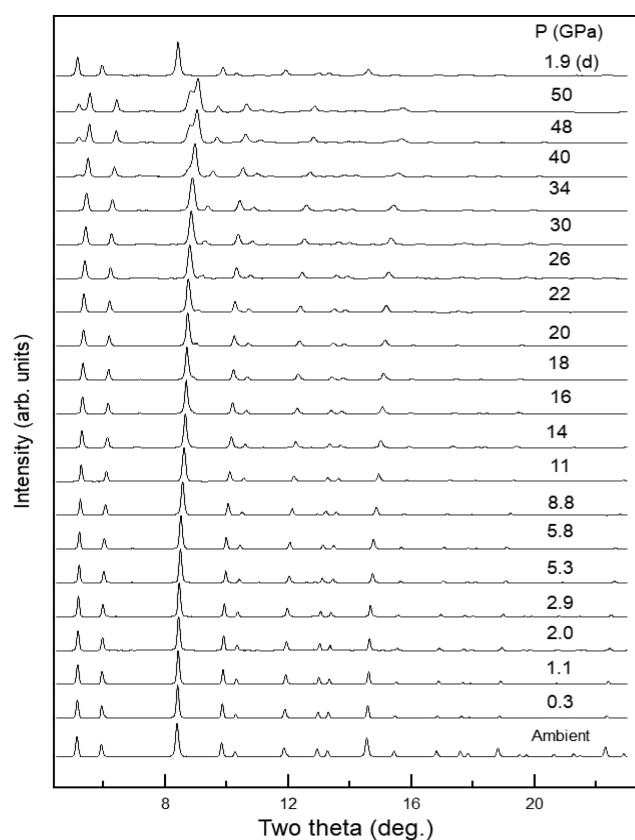


Figure 1. Evolution of XRD patterns with pressure increase for TiNiSn. The XRD pattern collected after releasing pressure is labeled as 1.6 (d).

visible as a doublet since the diffraction line corresponding to the Ne pressure-transmitting medium also merges with the sample peaks.³² However, above 40 GPa, the intensity of the asymmetric shoulder peak to the left of the (220) peak increases significantly more prevalently as pressure is increased to 50 GPa. Figure 2a shows the Le Bail fitting for the low- and high-pressure phases. To elucidate other smaller XRD peaks that begin to emerge, Figure 2b depicts the XRD patterns corresponding to 34, 40, 48, and 50 GPa separately to enhance the visibility of smaller XRD peaks.

Elastic tensor analysis has been done to check the mechanical stability in the investigated compound, TiNiSn. The calculated elastic tensor for the cubic system is given in Table S1. All the elastic constants are positive and satisfy Born's mechanical stability criteria.³³ The other elastic properties (e.g., elastic moduli and Debye temperature) are calculated using the Hill approximation.³⁴ The calculated bulk modulus is 130.78 GPa, and the Poisson ratio is 0.27. This value of Poisson ratio indicates the ductile nature of TiNiSn. The Debye temperature is found to be 506.23 K, which has not been experimentally determined, as of this publication. This is a very important parameter which links the thermodynamic properties to phonon-based properties.

The XRD patterns can be indexed well solely to the ambient pressure structure up to 20 GPa. In the pressure range of 20–40 GPa, the XRD patterns reveal that this structure remains as a major phase in addition to the evolving high-pressure orthorhombic phase with space group $Cmcm$ (No. 63). The high-pressure phase becomes prominent around 40 GPa. In order to obtain lattice parameters as a function of pressure, Le

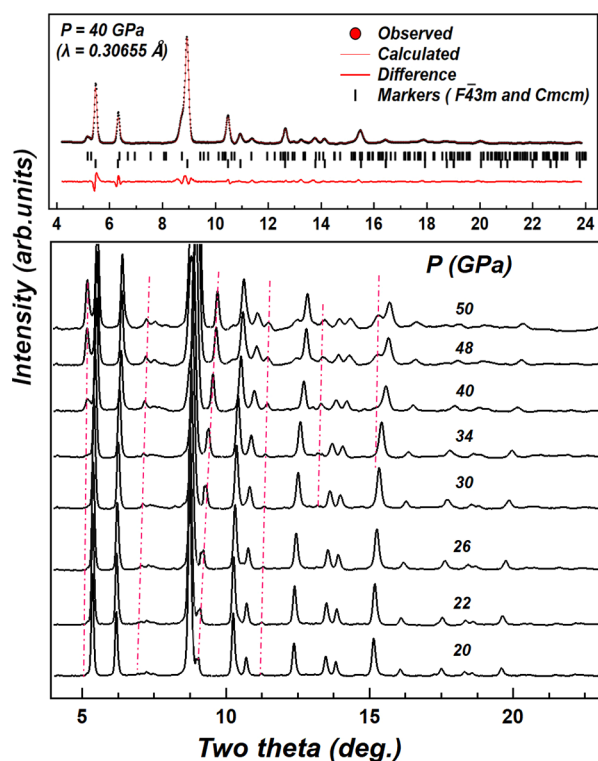


Figure 2. (a) Le Bail analysis at 40 GPa showing the cubic structure described by the $F\bar{4}3m$ space group and the orthorhombic structure described by the $Cmcm$ space group. (b) Expanded view of XRD patterns from 20 to 50 GPa revealing the appearance of several new peaks at 2θ angles 5.4° , 6.7° , and 11.1° , corresponding to the high-pressure phase. The peak at 8.5° is a doublet consisting of the Ne pressure-transmitting medium peak and a sample peak which becomes predominant at 50 GPa.

Bail analysis was performed on each XRD pattern up to the maximal pressure.^{35,36}

Once this analysis was performed on each XRD pattern corresponding to the entire pressure range for the ambient crystal structure, the lattice parameter, a , could be extracted and is displayed in Table S2a alongside the calculated unit-cell volume, V . Even though the high-pressure phase starts to emerge around 20 GPa, the cell parameters (and V) could be obtained only above 30 GPa (for the high-pressure phase) and are shown in Table S2b. Figure 3 shows a plot of V as a function of increasing pressure, which agrees well with the DFT calculations over the entire pressure range. The smooth decrease in V with compression indicates a reduction, as expected for the TiNiSn sample.

To understand the mechanical properties of TiNiSn, the P – V data can be fit to the BM-EOS, which allows determination of the bulk modulus. The BM-EOS is represented by the following equation:

$$P(V) = \frac{3K_0}{2} \left[\left(\frac{V_0}{V} \right)^{7/3} - \left(\frac{V_0}{V} \right)^{5/3} \right] \left\{ 1 + \frac{3}{4} (K'_0 - 4) \left[\left(\frac{V_0}{V} \right)^{2/3} - 1 \right] \right\} \quad (2)$$

where V_0 represents the zero-pressure volume, V represents the unit-cell volume, K_0 represents the bulk modulus, and K'_0 represents the pressure derivative of the bulk modulus.³⁷

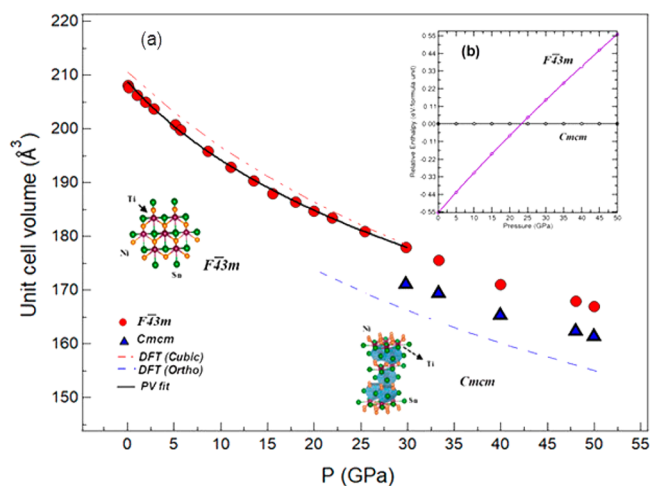


Figure 3. (a) Unit-cell volume as a function of increasing pressure for $F\bar{4}3m$ and $Cmcm$ phases. Red circles and blue triangles represent experimental data. The solid line represents a fit to the third-order Birch–Murnaghan equation of state (BM-EOS) using experimental data. Dotted/dashed lines represent density functional theory calculations. Inset (b) shows the enthalpy plot for low-pressure ($F\bar{4}3m$) and high-pressure ($Cmcm$) crystal structures.

The initial volume parameter was fixed to the ambient pressure value, $V_0 = 208.9 \text{ \AA}^3$, determined from the lattice parameter extracted from the ambient-pressure XRD pattern. This value agrees well with the values determined from DFT calculations of this study for GGA and local-density approximation (LDA), 209.6 and 196.1 \AA^3 , respectively. The optimized value of the bulk modulus from the fit to the third-order BM-EOS is provided in Table S3 as $K_0 = 106(9) \text{ GPa}$. Additionally, from a modified version of eq 2, the linear moduli for the a , b , and c axes can be determined and are shown in Table S3b. In the high-pressure phase, these moduli reveal an anisotropy between the a and c axes and the b axis. Specifically, the values of $M_{0,a}$ and $M_{0,c}$ are much more similar than $M_{0,b}$, indicating an anisotropy in compression strength where the b axis direction is softer than the a and c axes.

As there are no experimental reports on the bulk modulus of TiNiSn, no direct comparison can be made with experimental values. However, a recent experimental study was performed on a related half-Heusler compound, TiCoSb, and the bulk modulus was reported as $166(6) \text{ GPa}$.²⁹ Additionally, theoretical values for the bulk modulus for TiNiSn were reported by Wang et al. and Hermet et al. as 122 and 120 GPa, respectively.^{18,30} Furthermore, the DFT calculations performed as part of this study determined a bulk modulus of 130.8 GPa, which agrees quite well with the experimental value of 106(9) GPa. Figure 3 displays the EOS determined both experimentally and by DFT calculation. Good agreement below 30 GPa in the lower pressure phase is clearly observed, and at elevated pressures, as the phase becomes more mixed, there is some deviation between experiment and calculation. This deviation above 30 GPa is likely due to the experimental values being influenced by the mixed-phase state compared to the DFT calculation for the pure orthorhombic phase. The high-pressure structural search eventually led to the cubic structure with $F\bar{4}3m$ space group having the lowest enthalpy, in agreement with the experiment. Under pressure, we could clearly see an orthorhombic structure with $Cmcm$ space group,

which becomes energetically more favorable around 20 GPa. This is in good agreement with the experimental observation.

We have used two different exchange-correlation functionals for full geometry optimization and found that the optimized parameters using GGA are in good accordance with experimental parameters. The electronic structure properties are shown in Figure 4. From the plots, it can be seen that

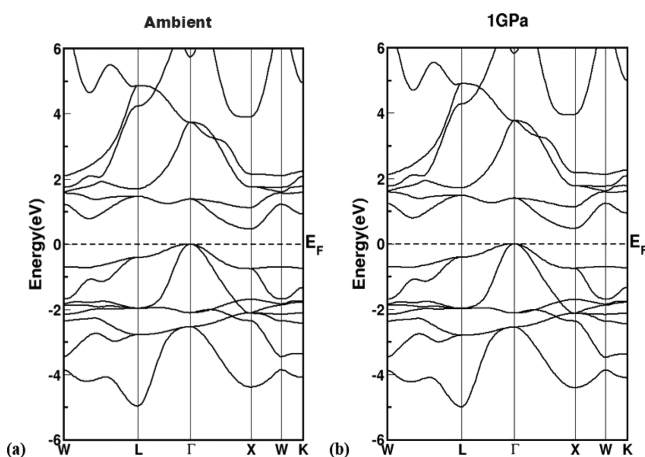


Figure 4. Calculated electronic band structure for TiNiSn at (a) ambient pressure and (b) 1 GPa.

TiNiSn is an indirect band gap semiconductor with a band gap of 0.46 eV. The existence of the valence band maxima at the Γ -point and the conduction band minima at the X-point is evidence for the same. The band profile in the valence band region near the Fermi level is more flattened than those present in the conduction band. This difference in band dispersion motivated us to investigate the thermoelectric nature of the present compound, which will be discussed in the next paragraphs.

All the thermoelectric properties are calculated under the relaxation time approximation. The calculated Seebeck coefficient for electrons is $-334.28 \mu\text{V K}^{-1}$ at 100 K, and the carrier concentration is around 10^{18} cm^{-3} . This value is in good accordance with the experimentally determined value of $-339 \mu\text{V K}^{-1}$. The electrical conductivity is on the order of $10^{17} \Omega^{-1} \text{ m}^{-1} \text{ s}^{-1}$. The power factor ($\sigma\alpha^2$) can be determined from the electrical conductivity (σ) and Seebeck coefficient (α) to characterize the energy that can be drawn from the system. Its value is on the order of $10^{10} \text{ W m}^{-1} \text{ K}^{-2} \text{ s}^{-1}$. All the calculated TE properties can be correlated to the electronic structure through band dispersion. The combination of flat and dispersive bands has effects on both the thermopower and the electrical conductivity scaled by relaxation time.

Combining the experimentally determined electrical resistivity, Seebeck coefficient, and thermal conductivity measurements up to 3.5 GPa (details are in the Supporting Information), the ZT value for TiNiSn can be calculated as a function of pressure using eq 1. Figure 5 shows the ZT normalized to the lowest pressure value as a function of increasing pressure. An overall increase in ZT is observed over the pressure range from 1 to 3 GPa, which levels out as pressure is increased further to 3.5 GPa. The initial increase in ZT value over the pressure range from 1 to 3 GPa is almost 15%. This 15% increase is despite the large increase in the thermal conductivity of over 60% and is likely due to the fairly large increase in the absolute value of the Seebeck coefficient

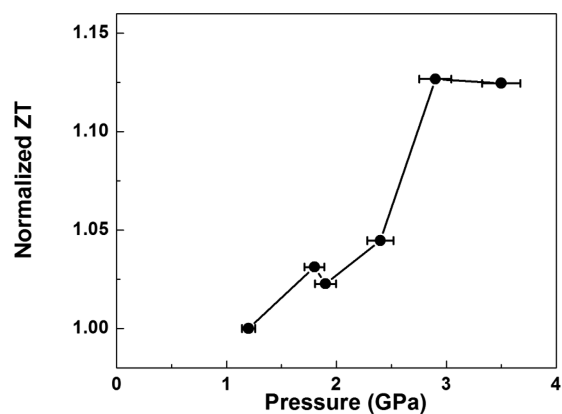


Figure 5. Dimensionless figure of merit ZT plotted as a normalized value as a function of increasing pressure for TiNiSn. An increase of almost 15% is observed over the pressure range from 1 to 3.0 GPa, with a plateau seemingly observed above 3.0 GPa.

over this same pressure range in addition to the electrical resistivity decrease. It is important to note that the thermoelectric measurements were performed under non-hydrostatic conditions, and while this may affect the results, it does not appear to influence the results in our experiments.³⁸ As reduction of the thermal conductivity through doping has been greatly explored for half-Heusler-type alloys, further exploration of doped alloys of TiNiSn at high-pressure conditions may be interesting to pursue. Nonetheless, measuring the properties of the pure TiNiSn alloys for understanding the pressure effect on the thermoelectric properties without distortions introduced through doping is important.

In conclusion, we have performed HP-XRD and DFT calculations on TiNiSn up to 50 GPa and observed stability of the ambient crystal structure up to 20 GPa. Above 20 GPa, there are distinct indications of a pressure-induced secondary crystal phase developing as pressure increases, evidenced by the emergence of several new diffraction peaks. Utilizing structure searching techniques, we have identified the high-pressure phase as an orthorhombic structure described by the *Cmcm* space group. The unit-cell volume as a function of pressure was fit to a third-order BM-EOS, yielding a bulk modulus value of 106(9) GPa, which agrees with the DFT calculations performed (130.8 GPa). Measurements of the thermoelectric properties at high-pressure conditions from 1 to 3.5 GPa were also presented for the first time. A 15% relative increase of ZT was observed with increasing pressure over the pressure range. The increase in thermoelectric efficiency of this material and the phase transition at high pressure promise that future studies of this material could be combined with chemical doping to establish further enhancement.

■ ASSOCIATED CONTENT

Supporting Information

The Supporting Information is available free of charge at <https://pubs.acs.org/doi/10.1021/acs.jpcllett.0c03609>.

Details of methods and high-pressure thermoelectric measurements, including Figures S1–S4 and Tables S1–S3 (PDF)

■ AUTHOR INFORMATION

Corresponding Author

Ravhi S. Kumar – Department of Physics, University of Nevada Las Vegas, Las Vegas, Nevada 89054, United States; Department of Physics, University of Illinois at Chicago, Chicago, Illinois 60607, United States; orcid.org/0000-0002-1967-1619; Email: ravhi@uic.edu

Authors

Jason L. Baker – Earth and Environmental Sciences Division, Los Alamos National Laboratory, Los Alamos, New Mexico 87545, United States

Changyong Park – High Pressure Collaborative Access Team, X-ray Science Division, Argonne National Laboratory, Argonne, Illinois 60439, United States; orcid.org/0000-0002-3363-5788

Curtis Kenney-Benson – High Pressure Collaborative Access Team, X-ray Science Division, Argonne National Laboratory, Argonne, Illinois 60439, United States

Vineet Kumar Sharma – Department of Physics, Indian Institute of Technology Hyderabad, Kandi Sanga Reddy 502 285, Telangana, India

V. Kanchana – Department of Physics, Indian Institute of Technology Hyderabad, Kandi Sanga Reddy 502 285, Telangana, India

G. Vaitheeswaran – School of Physics, University of Hyderabad, Hyderabad 500 046, Telangana, India; orcid.org/0000-0002-2320-7667

Chris J. Pickard – Department of Materials Science and Metallurgy, University of Cambridge, Cambridge CB3 0FS, U.K.

Andrew Cornelius – Department of Physics, University of Nevada Las Vegas, Las Vegas, Nevada 89054, United States

Nenad Velisavljevic – High Pressure Collaborative Access Team, X-ray Science Division, Argonne National Laboratory, Argonne, Illinois 60439, United States; Physics Division, Lawrence Livermore National Laboratory, Livermore, California 94550, United States

Complete contact information is available at:

<https://pubs.acs.org/10.1021/acs.jpcllett.0c03609>

Notes

The authors declare no competing financial interest.

■ ACKNOWLEDGMENTS

Portions of this work were performed at HPCAT (Sector 16), Advanced Photon Source (APS), Argonne National Laboratory. HPCAT operations are supported by DOE-NNSA's Office of Experimental Sciences. Support by CDAC, DOE-NNSA through grant number DE-NA0003975 is acknowledged. V. Sharma would like to acknowledge MoE for fellowship and IIT Hyderabad for providing computational facilities. V. Kanchana would like to acknowledge IIT Hyderabad for providing computational facilities. V. Kanchana would like to acknowledge BRNS project with sanction no. (58/14/13/2019-BRNS). The APS is a U.S. Department of Energy (DOE) Office of Science User Facility operated for the DOE Office of Science by Argonne National Laboratory under Contract No. DE-AC02-06CH11357. G.V. acknowledge CMSD, University of Hyderabad, for providing the computational facility. Portions of this work were performed under the

auspices of the U.S. DOE by Lawrence Livermore National Laboratory under Contract No. DE-AC52-07NA27344.

■ REFERENCES

- (1) Sagotra, A. K.; Errandonea, D.; Cazorla, C. Mechanocaloric Effects in Superionic Thin Films from Atomistic Simulations. *Nat. Commun.* **2017**, *8*, 963.
- (2) Schmidt, G. R.; Wiley, R. L.; Richardson, R. L. NASA's Program for Radioisotope Power System Research and Development. *AIP Conf. Proc.* **2005**, *746*, 429–436.
- (3) Huang, L.; Zhang, Q.; Yuan, B.; Lai, X.; Yan, X.; Ren, Z. Recent Progress in Half-Heusler Thermoelectric Materials. *Mater. Res. Bull.* **2016**, *76*, 107–112.
- (4) Poon, S. J.; Wu, D.; Zhu, S.; Xie, W.; Tritt, T. M.; Thomas, P.; Venkatasubramanian, R. Half-Heusler Phases and Nanocomposites as Emerging High-ZT Thermoelectric Materials. *J. Mater. Res.* **2011**, *26*, 2795–2802.
- (5) Liu, W. S.; Yan, X.; Chen, G.; Ren, Z. F. Recent Advances in Thermoelectric Nanocomposites. *Nano Energy* **2012**, *1*, 42–56.
- (6) Xie, W.; Weidenkaff, A.; Tang, X. F.; Zhang, Q. J.; Poon, J.; Tritt, T. M. Recent Advances in Nanostructured Thermoelectric Half-Heusler Compounds. *Nanomaterials* **2012**, *2*, 379–412.
- (7) Chen, S.; Ren, Z. F. Recent Progress of Half-Heusler for Moderate Temperature Thermoelectric Applications. *Mater. Today* **2013**, *16* (10), 387–395.
- (8) Bos, J. W. G.; Downie, R. A. Half-Heusler Thermoelectrics: a Complex Class of Materials. *J. Phys.: Condens. Matter* **2014**, *26*, 433201.
- (9) Zhu, T.; Fu, C.; Xie, H.; Liu, Y.; Zhao, X. High Efficiency Half-Heusler Thermoelectric Materials for Energy Harvesting. *Adv. Energy Mater.* **2015**, *5*, 1500588.
- (10) Rogl, G.; Grytsiv, A.; Failamani, F.; Hochenhofer, M.; Bauer, E.; Rogl, P. Attempts to Further Enhance ZT in Skutterudites via Nano-Composites. *J. Alloys Compd.* **2017**, *695*, 682–696.
- (11) Shi, X.; Yang, J.; Salvador, J.; Chi, M.; Cho, J. Y.; Wang, H.; Bai, S.; Yang, J.; Zhang, W.; Chen, L. Multiple-Filled Skutterudites: High Thermoelectric Figure of Merit Through Separately Optimizing Electrical and Thermal Transports. *J. Am. Chem. Soc.* **2011**, *133* (20), 7837–7846.
- (12) Zhao, L. D.; Hao, S.; Lo, L. H.; Wu, C. I.; Zhou, X.; Lee, Y.; Li, H.; Biswas, K.; Hogan, T. P.; Uher, C.; et al. High Thermoelectric Performance via Hierarchical Compositionally Alloyed Nanostructures. *J. Am. Chem. Soc.* **2013**, *135* (19), 7364–7370.
- (13) Lee, Y.; Lo, S. H.; Androulakis, J.; Wu, C. I.; Zhao, L. D.; Chung, D. Y.; Hogan, T. P.; Dravid, V. P.; Kanatzidis, M. G. High-Performance Tellurium-Free Thermoelectrics: Allscale Hierarchical Structuring of P-Type PbSe-MSe Systems (M = Ca, Sr, Ba). *J. Am. Chem. Soc.* **2013**, *135* (13), 5152–5160.
- (14) Pei, Y. L.; Liu, Y. Electrical and Thermal Transport Properties of Pb-Based Chalcogenides: PbTe, PbSe, and PbS. *J. Alloys Compd.* **2012**, *514*, 40–44.
- (15) Thwaha, S.; Zhu, J.; Yan, Y.; Li, B. A Comprehensive Review of Thermoelectric Technology: Materials, Applications, Modelling, and Performance Improvement. *Renewable Sustainable Energy Rev.* **2016**, *65*, 698–726.
- (16) Nozariasbmarz, A.; Agarwal, A.; Coutant, Z. A.; Hall, M. J.; Liu, J.; Liu, R.; Malhotra, A.; Norouzzadeh, P.; Öztürk, M. C.; et al. Thermoelectric Silicides: A Review. *Jpn. J. Appl. Phys.* **2017**, *56*, 05DA04.
- (17) Tobola, J.; Pierre, J.; Kaprzyk, S.; Skolozdra, R. V.; Kouacou, M. A. Crossover from Semiconductor to Magnetic Metal in Semi-Heusler Phases as a Function of Valence Electron Concentration. *J. Phys.: Condens. Matter* **1998**, *10*, 1013.
- (18) Wang, L. L.; Miao, L.; Wang, Z. Y.; Wei, W.; Xiong, R.; Liu, H. J.; Shi, J.; Tang, X. F. Thermoelectric Performance of Half-Heusler Compounds TiNiSn and TiCoSb. *J. Appl. Phys.* **2009**, *105* (1), 013709.
- (19) Bhattacharya, S.; Pope, A. L.; Littleton, R. T.; Tritt, T. M.; Ponnambalam, V.; Xia, Y.; Poon, S. J. Effect of Sb Doping on the

Thermoelectric Properties of Ti-Based Half-Heusler Compounds, TiNiSn_{1-x}Sbx. *Appl. Phys. Lett.* **2000**, *77*, 2476–2478.

(20) Hohl, H.; Ramirez, A. P.; Goldmann, C.; Ernst, G.; Wölfing, B.; Bucher, E. Efficient Dopants for ZrNiSn-Based Thermoelectric Materials. *J. Phys.: Condens. Matter* **1999**, *11*, 1697–1710.

(21) Kurosaki, K.; Maekawa, T.; Muta, H.; Yamanaka, S. Effect of Spark Plasma Sintering Temperature on Thermoelectric Properties of (Ti,Zr,Hf)NiSn Half-Heusler Compounds. *J. Alloys Compd.* **2005**, *397*, 296–299.

(22) Hohl, H.; Ramirez, A. P.; Kaefer, W.; Fess, K.; Thurner, Ch; Kloc, Ch; Bucher, E. A New Class of Materials with Promising Thermoelectric Properties: MNiSn (M = Ti, Zr, Hf). *Mater. Res. Soc. Symp. Proc.* **1997**, *478*, 109.

(23) Sakurada, S.; Shutoh, N. Effect of Ti Substitution on the Thermoelectric Properties of (Zr,Hf)NiSn Half-Heusler Compounds. *Appl. Phys. Lett.* **2005**, *86*, 082105.

(24) Uher, C.; Yang, J.; Hu, S.; Morelli, D. T.; Meisner, G. P. Transport Properties of Pure and Doped MNiSn (M = Zr, Hf). *Phys. Rev. B: Condens. Matter Mater. Phys.* **1999**, *59*, 8615.

(25) Ovsyannikov, S. V.; Shchennikov, V. V. Pressure-Tuned Colossal Improvement of Thermoelectric Efficiency of PbTe. *Appl. Phys. Lett.* **2007**, *90*, 122103.

(26) Baker, J.; Kumar, R.; Park, C.; Kenney-Benson, C.; Cornelius, A.; Velisavljevic, N. Giant Pressure-Induced Enhancement of Seebeck Coefficient and Thermoelectric Efficiency in SnTe. *ChemPhysChem* **2017**, *18*, 3315–3319.

(27) Baker, J.; Kumar, R.; Park, C.; Kenney-Benson, C.; Cornelius, A.; Velisavljevic, N. High-Pressure Seebeck Coefficients and Thermoelectric Behaviors of Bi and PbTe Measured Using a Paris-Edinburgh Cell. *J. Synchrotron Radiat.* **2016**, *23*, 1368–1378.

(28) Zhao, L. D.; Lo, S. H.; Zhang, Y.; Sun, H.; Tan, G.; Uher, C.; Wolverton, C.; Dravid, V. P.; Kanatzidis, M. G. Ultralow Thermal Conductivity and High Thermoelectric Figure of Merit in SnSe Crystals. *Nature* **2014**, *508*, 373–377.

(29) Baker, J. L.; Kumar, R.; Park, C.; Velisavljevic, N.; Cornelius, A. Compressibility and Thermoelectric Behavior of TiCoSb Half-Heusler Compound at High Pressures. *Intermetallics* **2018**, *95*, 137–143.

(30) Hermet, P.; Niedziolka, K.; Jund, P. A First-Principles Investigation of the Thermodynamic and Mechanical Properties of Ni-Ti-Sn Heusler and Half-Heusler Materials. *RSC Adv.* **2013**, *3*, 22176–22184.

(31) Jeitschko, W. Transition metal stannides with MgAgAs and MnCu₂Al type structure. *Metallurgical Trans.* **1970**, *1*, 3159–3162.

(32) Hemley, R. J.; Zha, C. S.; Jephcoat, A. P.; Mao, H. K.; Finger, L. W.; Cox, D. E. X-Ray Diffraction and Equation of State of Solid Neon to 110 GPa. *Phys. Rev. B: Condens. Matter Mater. Phys.* **1989**, *39*, 11820.

(33) Mouhat, F.; Coudert, F.-X. Necessary and Sufficient Elastic Stability Conditions in Various Crystal Systems. *Phys. Rev. B: Condens. Matter Mater. Phys.* **2014**, *90*, 224104.

(34) Hill, R. The Elastic Behavior of a Crystalline Aggregate. *Proc. Phys. Soc., London, Sect. A* **1952**, *65*, 349.

(35) Le Bail, A. Whole Powder Pattern Decomposition Methods and Applications: A Retrospection. *Powder Diffr.* **2005**, *20* (4), 316–326.

(36) Le Bail, A. Extracting Structure Factors from Powder Diffraction Data by Iterating Full Pattern Profile Fitting. In *Accuracy in Powder Diffraction II*; Prince, E., Stalick, J. K., Eds.; NIST Special Publication 846; National Institute of Standards and Technology: Gaithersburg, MD, 1992; p 213.

(37) Birch, F. The Effect of Pressure Upon the Elastic Parameters of Isotropic Solids, According to Murnaghan's Theory of Finite Strain. *J. Appl. Phys.* **1938**, *9*, 279.

(38) Morozova, N. V.; Korobeinikov, I. V.; Ovsyannikov, S. V. Strategies and Challenges of High-Pressure Methods Applied to Thermoelectric Materials. *J. Appl. Phys.* **2019**, *125*, 220901.